

## KINEMATIC DISTANCES OF GALACTIC PLANETARY NEBULAE

A. Y. YANG<sup>1,2</sup>, W. W. TIAN<sup>1,2,3</sup>, H. ZHU<sup>1,2</sup>, D. A. LEAHY<sup>3</sup>, D. WU<sup>1,4,5</sup><sup>1</sup>Key Laboratory of Optical Astronomy, National Astronomical Observatories,  
Chinese Academy of Sciences, Beijing 100012, China<sup>2</sup>University of Chinese Academy of Science, 19A Yuquan Road, Beijing 100049, China<sup>3</sup>Department of Physics & Astronomy, University of Calgary, Calgary, Alberta T2N 1N4, Canada<sup>4</sup>College of Information Science and Technology, Beijing Normal University, Beijing 100875, China<sup>5</sup>Beijing Key Laboratory of Digital Preservation and Virtual Reality for Cultural Heritage, Beijing 100875, China*Draft version January 14, 2016*

## ABSTRACT

We construct H I absorption spectra for 18 planetary nebulae (PNe) and their background sources using the data from the International Galactic Plane Survey. We estimate the kinematic distances of these PNe, among which 15 objects' kinematic distances are obtained for the first time. The distance uncertainties of 13 PNe range from 10% to 50%, which is a significant improvement with uncertainties of a factor two or three smaller than most of previous distance measurements. We confirm that PN G030.2–00.1 is not a PN because of its large distance found here.

*Subject headings:* (ISM:) planetary nebulae: general—ISM: kinematics and dynamics—ISM: clouds—stars: distances

## 1. INTRODUCTION

Distances, as a basic physical parameter of planetary nebulae (PNe), are crucial to study their size, luminosity, ionized mass, formation rate, space density and Galactic distribution. However, distances are still not well determined for the majority of total  $\sim 3500$  PNe (Kwitter et al. 2014). For an individual PN, different methods may lead to different distances. So far, there are only about thirty PNe having their distance measurements with uncertainties less than 20%.

Nine popular methods have been used to measure the distances of PNe, including trigonometric parallax (e.g., Harris et al. 2007), cluster member (e.g., Jacoby et al. 1997), expansion parallax (e.g., Terzian 1997), spectroscopic parallax (e.g., Ciardullo et al. 1999), reddening (e.g., Gathier et al. 1986b), Na D absorption (e.g., Napiwotzki & Schoenberger 1995), determinations of central star gravities (e.g., Mendez et al. 1988), statistical method (revised Shklovsky method, e.g., Shklovskii 1956) and kinematics method (e.g., Gathier et al. 1986a).

Hydrogen is the most abundant element in the universe and H I atom clouds are broadly distributed in the Milky Way (Dickey & Lockman 1990). The 21 cm H I absorption line has been widely used to measure kinematic distances of H I clouds and radio strong sources associated. When a H I cloud is located in front of or behind a strong radio source, we are usually able to detect a H I absorption feature or only an emission line from the cloud. The velocity of the emission/absorption feature can be converted into a distance based on the axisymmetric rotation curve model for the Galaxy. The distance or distance limit of the source can be estimated from the distance of the H I cloud. However, this method faces two main challenges. One is the kinematic distance ambiguity (KDA) for sources located inside the solar circle, as each radial velocity along given line of sight corresponds to two distances equally spaced on either side of

the tangent point. The KDA usually can be solved by integrated consideration of H I absorption/self-absorption, CO emission and H I absorption of background sources. Another challenge is to construct a reliable H I absorption spectrum to a radio source due to the uneven H I background in the Galaxy. In order to minimize the second effect, Tian et al. (2007) and Leahy & Tian (2008) developed revised methods to construct H I absorption spectra. The methods have been applied to several types of Galactic objects successfully, e.g., PNe (Zhu et al. 2013), supernova remnants and H II regions (e.g., Leahy & Tian 2008; Tian & Leahy 2008).

In this paper, we systematically construct the H I absorption spectra of PNe which are located in the sky region of the International Galactic Plane Survey (IGPS). H I absorption features in the spectra are used to determine the PNe's distances. This paper is organized as follows: the data and the revised methods are introduced in Section 2. In Section 3, we apply the methods to estimate individual PN distance. Summary is given in Section 4.

## 2. DATA ANALYSIS

## 2.1. Data

The 1420 MHz radio continuum and H I-line emission data come from IGPS (the Very Large Array Galactic Plane Survey (VGPS) (Stil et al. 2006), the Southern Galactic Plane Survey (SGPS) (McClure-Griffiths et al. 2005), and the Canadian Galactic Plane Survey (CGPS) (Taylor et al. 2003)). The project surveys the Galactic disk from longitudes  $18^\circ$  to  $67^\circ$ ,  $255^\circ$  to  $357^\circ$  and  $65^\circ$  to  $175^\circ$ , respectively. For CGPS, the continuum image at 1420 MHz has a spacial resolution of  $1'$  and H I spectra line images have a resolution of  $1' \times 1' \times 1.56 \text{ km s}^{-1}$ . At declination  $\delta$ , the synthesized beam is  $49'' \times 49'' \csc \delta$  for 1420 MHz and  $58'' \times 58'' \csc \delta \times 1.32 \text{ km s}^{-1}$  for H I in the survey of CGPS. SGPS has a resolution  $100''$  for continuum and  $\sim 2' \times 2' \times 1 \text{ km s}^{-1}$  for H

TABLE 1  
INFORMATION OF PNE AND BACKGROUND SOURCES

PN G Name	$l$ °	$b$ °	$S_{1.4\text{GHz}}$ mJy	Survey	Ref.	Background $l$	Sources $b$
G020.9−01.1	20.999	−1.125	249.0±7.5	V	CK98	21.345 21.500	−0.630 −0.885
G029.0+00.4	29.079	0.454	159.0±15	V	CK98	28.800 28.825 29.098	0.175 −0.230 0.545
G030.2−00.1	30.234	−0.139	... <sup>a</sup>	V	A11	29.930 30.535 30.685 29.960	−0.055 0.020 −0.260 −0.020
G051.5+00.2	51.509	0.167	84.0	V	LCY05	51.775 50.625 50.950	0.800 −0.030 0.850
G052.1+01.0	52.099	1.043	455.1±13.7	V	IPHAS09	52.235 52.750	0.745 0.335
G055.5−00.5	55.507	−0.558	84.1±2.6	V	CK98	55.525 55.995 55.775	−1.150 −1.195 −0.250
G069.7−00.0	69.800	0.004	87.1±2.6	V	CK98	68.755 70.155	0.275 0.090
G070.7+01.2	70.674	1.192	949.6±33.4	C	IPHAS09	71.225 70.690 70.600	1.445 0.630 1.380
G084.9−03.4	84.930	−3.496	1373±41	C	CK98	85.120 84.445	−3.100 −2.915
G089.0+00.3	89.002	0.376	260.5±7.8	C	IPHAS09	88.825 88.465 89.650	0.925 0.004 0.925
G107.8+02.3	107.845	2.314	581±22.8	C	IPHAS09	108.755	2.575
G138.8+02.8	38.816	2.805	153.1± 5.8	C	CK98	138.795	2.140
G147.4−02.3	147.401	−2.307	77.8± 2.4	C	IPHAS09	146.625 147.950	−2.690 −2.645
G169.7−00.1	169.653	−0.077	135.3±5.1	C	IPHAS09	169.080 170.330	−0.245 −0.225
G259.1+00.9	259.149	0.940	345±12	S	CK98	257.902 257.913	0.844 0.655
G333.9+00.6	333.930	0.686	294.8±9.7	S	BPF11	333.723 332.967	0.377 0.777
G352.6+00.1	352.675	0.144	378±38	S	CK98	352.588 351.616 353.408	−0.167 0.177 −0.355
G352.8−00.2	352.828	−0.259	474±47	S	CK98	352.588 352.854 353.408	−0.167 −0.189 −0.355

NOTE. — The first three columns give the name and Galactic coordinates. Column (4) gives the flux density at 1.4 GHz. The survey names and references are given in the next two columns. The final two columns give the Galactic coordinates of background sources. References related in table are as follow: IPHAS09-Viironen et al. (2009), CK98-Condon & Kaplan (1998), LCY05-Luo et al. (2005), BPF11-Bojčić et al. (2011), A11-Anderson et al. (2011). a—the flux at 8.7 GHz is 752 mJy for PN G030.2−00.1.

I data. The  $^{13}\text{CO}$  spectral line data from the Galactic Ring Survey of the Five College Radio Astronomical Observatory (FCRAO) 14 m telescope (Jackson et al. 2006) has an angular and spectral resolution of  $46''$  and  $0.21 \text{ km s}^{-1}$  at longitudes from  $18^\circ$  to  $52^\circ$  and latitudes between  $-1^\circ$  and  $1^\circ$ . The  $^{12}\text{CO}$  ( $J=1-0$ ) spectral line data from the FCRAO CO Survey of the Outer Galaxy has an angular and spectral resolution of  $45''$  and  $0.98 \text{ km s}^{-1}$  between Galactic longitudes  $102.49^\circ - 141.54^\circ$  and latitudes  $-3.03^\circ - 5.41^\circ$  (Heyer & Terebey 1998).

In this work, we construct the H I absorption spectra of the PNe with flux density larger than 50 mJy at 1420 MHz in the IGPS. By checking their H I spectra one by one visually, 18 of them show reliable absorption features. We analyze the 18 PNe in this paper. For

each PN, at least one bright nearby background source has been chosen as a comparison with the PN in order to understand the PN's H I absorption spectrum. The parameters of 18 PNe and their background sources are shown in Table 2.1.

## 2.2. To obtain a reliable H I absorption spectrum

Based on the knowledge of radiation transfer, the brightness temperature of source ( $T_{\text{on}}$ ) and background ( $T_{\text{off}}$ ) that have continuum emission subtracted can be determined by the equations:

$$T_{\text{on}}(\nu) = T_{\text{B}}(\nu)(1 - e^{-\tau(\nu)}) + T_{\text{S}}^{\text{C}}(e^{-\tau_{\text{c}}(\nu)} - 1) \quad (1)$$

$$T_{\text{off}}(\nu) = T_{\text{B}}(\nu)(1 - e^{-\tau(\nu)}) + T_{\text{bg}}^{\text{C}}(e^{-\tau_{\text{c}}(\nu)} - 1) \quad (2)$$

So, we can obtain the absorption spectrum of H I,

$$e^{-\tau_c(\nu)} = 1 - \frac{T_{\text{off}}(\nu) - T_{\text{on}}(\nu)}{T_S^C - T_{\text{bg}}^C}, \quad (3)$$

Where,  $T_B(\nu)$  is the spin temperature of H I cloud,  $T_S^C$  and  $T_{\text{bg}}^C$  are the continuum brightness temperatures of source and background. The H I absorption spectrum is usually represented by  $e^{-\tau_c(\nu)}$  or sometimes by  $\tau_c$ .

To construct a H I absorption spectrum, traditionally one usually chooses the source and background regions separately. This could increase the possibility of false absorption spectrum caused by the different distributions of H I clouds along the two lines of sight. Nevertheless, Tian et al. (2007) and Leahy & Tian (2008) proposed revised methods by selecting the background region directly surrounding the source region to minimize the possibility of a false H I absorption spectrum. In addition, they extracted CO emission spectrum in the source direction and constructed H I absorption spectra of nearby strong background sources with their angular separation not exceeding  $1^\circ$  from target source to understand the target source's absorption spectrum better. What's more, when it is possible, H I self absorption resulting from cold H I cloud absorbing emission from background warm H I cloud at the same velocity has been used to reduce the KDA problem in the methods (e.g., Leahy & Tian 2010; Tian et al. 2010).

### 3. KINEMATIC DISTANCE MEASUREMENT TO PLANETARY NEBULAE

#### 3.1. The model

The methods of determining distances are based on the flat Galactic circular rotation curve model. For a given PN at a distance  $d$  from the Sun in the direction of  $(l, b)$  in Galactic coordinates, the relation between the heliocentric distance  $d$  and the galactocentric distance  $R$  can be written as

$$R^2 = R_0^2 + d^2 \cos^2 b - 2R_0 d \cos b \cos l, \quad (4)$$

where  $R_0 = 7.62 \pm 0.32$  kpc (Eisenhauer et al. 2005), the distance to the Galactic center from the Sun. However,  $R_0$  is still uncertain (e.g. Bovy et al. 2012). Assuming circular orbits, the rotation velocity  $V_R$  at galactocentric distance  $R$  is given by

$$V_R = \frac{R}{R_0} \left( \frac{V_r}{\cos b \sin l} + V_0 \right), \quad (5)$$

where  $V_r$  is the radial velocity corresponding to the Local Standard of Rest (LSR), and  $V_0 = 220$  km s $^{-1}$  is the IAU adopted velocity at the LSR. In this work, we focus on the relation between the heliocentric distance  $d$  and the radial velocity  $V_r$ . Since  $d$  can be expressed by

$$d = \frac{R_0 \cos l \pm \sqrt{R^2 - (R_0 \sin l)^2}}{\cos b}, \quad (6)$$

where  $R$  is related to  $V_r$  in equation (5), the heliocentric distance  $d$  can be written as a function of the radial velocity  $V_r$ , which has different forms of expression in the four quadrants of the Galactic coordinates, see Fig. 1. In general, we analyze the spectra of PNe and their background sources to determine the kinematic distances of

PNe assuming  $V_R = V_0$ . In some special cases, when the maximum observed radial velocity (tangent point velocity) in the PN spectrum is much larger than the expected value, i.e.,  $V_R > V_0$ , we consider  $V_R$  linearly increasing from  $V_0 = 220$  km s $^{-1}$  to  $V_R$  as  $R$  reduces to the value at the tangent point. The same situation has been discussed in Leahy et al. (2008). We note that Reid et al. (2007) had updated the value  $V_0/R_0$  with  $V_0 = 224$  km s $^{-1}$  and  $V_R = 242$  km s $^{-1}$ . Reid et al. (2009) also found a higher rotation velocity of  $V_0 = 254 \pm 16$  km s $^{-1}$  by measuring the trigonometric parallaxes and proper motions of masers with the Very Long Baseline Array data. Likewise, Leahy et al. (2008) and Levine et al. (2008) suggested a higher rotation velocity at longitude near  $53^\circ$ .

#### 3.2. Application to Planetary Nebula

We estimate distances of 18 PNe by taking  $3\sigma$  as the minimum level of significance for the detection of a H I absorption feature, where  $\sigma$  is the standard deviation calculated from the no emission baseline of PN H I spectrum. The distance uncertainty includes that caused by an average random velocity of H I clouds, i.e.,  $\sim 6$  km s $^{-1}$  (Crovisier 1978; Shaver et al. 1982; Anantharamiah et al. 1984). For each PN, at least one bright background source within an angular separation of  $1^\circ$  from the PNe has been chosen. The spectra are used to compare with the PN's in order to understand the PN's absorption spectrum. The 1420 MHz continuum images of both PNe and background sources are displayed in Fig. 2 to Fig. 19, together with their H I absorption spectra. The distance for each individual PN is discussed below, taking  $R_0 = 7.62$  kpc.

##### PN G020.9-01.1 (Fig. 2):

Fig. 2 shows the 1420 MHz continuum image and H I spectra of PN G020.9-01.1 and its nearby background sources (G021.3-0.63, G021.5-0.89). The PN is fainter in radio than both G021.3-0.63 and G021.5-0.89 so that the PN H I absorption spectrum shows more noise than the others. Absence of absorption at the tangent point velocity ( $\sim 100$  km s $^{-1}$ ) for both PN G020.9-01.1 and G021.5-0.89 implies they are likely located in front of the tangent point ( $7.1 \pm 0.6$  kpc). The spectrum of G021.3-0.63 shows absorption features at  $105$  km s $^{-1}$  and negative velocities, which supports that this source is further than both PN G020.9-01.1 and G021.5-0.89. The absorption feature at  $62$  km s $^{-1}$  is probably not real since the absorption is very close to  $3\sigma$ . The reliable absorption feature at  $45$  km s $^{-1}$  ( $e^{-\tau} = 0.44$ ) indicates a lower limit distance of  $3.1 \pm 0.3$  kpc for the PN, i.e., the nearside distance for this velocity.

For PN G020.9-01.1, Cazetta & Maciel (2001) found a distance of  $2.4$  kpc based on the relation between distance and the surface gravity of central star of PN ( $d^2 \propto M_\odot F_* g^{-1} 10^{0.4V_0}$ ). This kinematic distance of  $3.1 \pm 0.3$  kpc is reasonably consistent with the surface gravity distance, and larger than previous statistical distances of  $1.75$  kpc by Cahn et al. (1992),  $1.66$  kpc by van de Steene & Zijlstra (1995),  $1.74$  kpc by Zhang (1995),  $2.29$  kpc by Stanghellini et al. (2008) and  $1.59$  kpc by Phillips (2004).

##### PN G029.0+00.4 (Fig. 3):

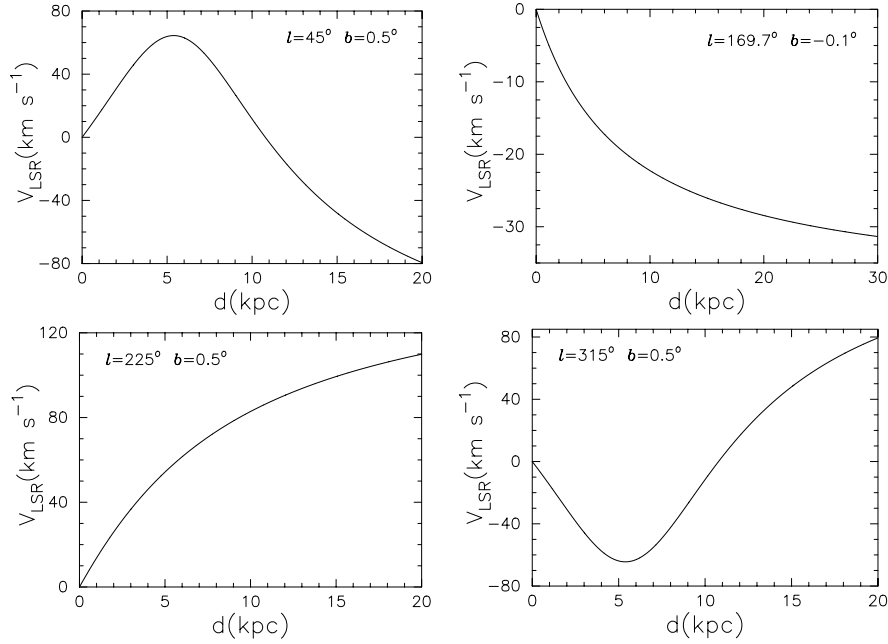


FIG. 1.— The relation between heliocentric distance  $d$  and radial velocity  $V_r$  in the four quadrants in the direction  $(l, b)$  in Galactic coordinates, using a Galactic circular rotation curve model and adopting a galactocentric distance of  $R_0=7.62$  kpc and a rotation velocity of  $V_0=220$  km s $^{-1}$ .

Although the background sources near PN G029.0+00.4 show clear absorption spectra, the PN spectrum is complex. The prominent emission at the tangent point ( $\sim 100$  km s $^{-1}$ ) and the absence of an absorption feature at the velocity in the PN spectrum indicate an upper limit distance of  $6.6 \pm 1.0$  kpc for the PN. One probable absorption feature at  $60$  km s $^{-1}$  implies a lower limit distance of  $3.5 \pm 0.3$  kpc.

For this PN, a distance of  $1.2$  kpc has been derived by Maciel (1984) assuming a relationship between the nebular ionized mass and radius, which is smaller than our result.

#### PN G030.2–00.1 (Fig. 4):

PN G030.2–00.1 is a PN candidate suggested by Anderson et al. (2011). The absorption features of the PN candidate and four H II regions appear up to the tangent point velocity ( $\sim 110$  km s $^{-1}$ ), which indicates all five objects are beyond the tangent point, i.e.,  $6.6 \pm 0.9$  kpc. The absence of absorption at negative velocity in the PN spectrum implies the PN is inside the solar circle ( $13.2 \pm 0.5$  kpc). The obvious absorption feature in the PN spectrum and absence of absorption in spectra of all background sources at  $40$  km s $^{-1}$  imply that the PN is likely beyond the far-side distance of  $40$  km s $^{-1}$ , i.e.,  $10.7 \pm 0.3$  kpc. Based on these information, the PN sits between  $10.7 \pm 0.3$  kpc and  $13.2 \pm 0.5$  kpc.

#### PN G051.5+00.2 (Fig. 5):

Based on the Galactic circular rotation curve model and the IAU adopted parameters of  $V_0=220$  km s $^{-1}$ , the tangent velocity  $V_\perp$  is expected to be  $48$  km s $^{-1}$ . This is much smaller than the observed value of  $V_\perp \simeq 70$  km s $^{-1}$  obtained from the H I emission spectrum in Fig. 5. This higher  $V_\perp$  could be due to spiral arm velocity perturbation near the tangent point in the direction of  $l=51.5^\circ$  (Dobbs et al. 2006). If  $V_\perp = 70$  km s $^{-1}$ , the rotation

velocity  $V_R$  would be as high as  $242$  km s $^{-1}$ . In fact, Levine et al. (2008) found a high rotation velocity of  $\sim 236$  km s $^{-1}$  at longitude near  $53^\circ$ . In addition, the high rotation velocity is also obtained in the H I spectra of PN G052.1+01.0 and PN G055.5–00.5. Altogether, we calculate the kinematic distance to the PN using  $R_0=7.62$  kpc,  $V_0=220$  km s $^{-1}$  and  $V_R=243$  km s $^{-1}$ .

The PN spectrum reveals absorptions appear up to the tangent point velocity, giving a lower limit distance of  $4.7 \pm 1.4$  kpc. The absence of any absorption feature at negative velocities in the PN spectrum means that the PN is within the solar circle, giving an upper limit distance of  $9.5 \pm 0.4$  kpc.

#### PN G052.1+01.0 (Fig. 6):

Similar to PN G051.5+00.2, the observed tangent point velocity of  $68$  km s $^{-1}$  from the PN H I spectrum is larger than the expected value of  $46$  km s $^{-1}$  when taking commonly used parameters of  $V_0=220$  km s $^{-1}$ . This leads to a rotation velocity up to  $V_R=242$  km s $^{-1}$ . Fig. 6 shows absorption features in the spectra of the PN and two H II regions (G052.2+0.75, G052.7+0.3) up to the tangent point velocity ( $68$  km s $^{-1}$ ), revealing all three objects are beyond the tangent point. So the lower limit distance for this PN is  $4.7 \pm 1.4$  kpc. Bright H I emission is detected at  $48$  km s $^{-1}$  in the three spectra, whereas the absorption feature at this velocity is detected only in the spectra of two H II regions. This implies that the PN is in front of H I at its far-side distance of  $5.6 \pm 0.8$  kpc.

#### PN G055.5–00.5 (Fig. 7):

The observed tangent point velocity ( $55$  km s $^{-1}$ ) in the PN spectrum is larger than the expected value ( $38$  km s $^{-1}$ ), which suggests that the rotation velocity is  $V_R=236$  km s $^{-1}$  at the tangent point. Absorption features at the tangent point velocity in the spectra of the PN

as well as three background sources (G055.5–01.1, G055.9–01.2 and G055.7–00.2) indicate that all four objects are beyond the tangent point. Therefore, the lower limit distance is  $4.3 \pm 1.5$  kpc for the PN. Absence of absorption in the PN spectrum at negative velocity implies that the PN is within the solar cycle. So we suggest that the distance of the PN is between  $4.3 \pm 1.5$  kpc and  $8.6 \pm 0.4$  kpc.

Giammanco et al. (2011) suggested a distance of  $2.9 \pm 0.4$  based on distance-extinction relationship in the direction toward the PN. Zhang (1995) derived a distance of 3.17 kpc by using the relation between the radio continuum surface brightness and the nebular radius. Stanghellini et al. (2008) obtained a distance of 3.68 kpc by the revised relation of ionized mass and optical thickness. So our lower limit distance of  $4.3 \pm 1.5$  kpc for the PN G055.5–00.5 is reasonable.

PN G069.7–00.0 (Fig. 8):

The PN spectrum has low S/N due to its low brightness. Significant absorption features are detected at the tangent point velocity and at negative velocities in the spectra of both the PN and its background sources, hinting that they are all beyond the solar circle ( $d = 5.3 \pm 0.7$  kpc). According to the noise level ( $3\sigma = 0.23$ ), the H I emission and absorption features at  $-64$  km  $s^{-1}$  reveal a lower limit distance of  $11.1 \pm 0.6$  kpc for the PN. The presence of H I emission at  $-73$  km  $s^{-1}$  and the absence of an absorption feature at the same velocity indicate an upper limit distance of  $12.0 \pm 0.7$  kpc. In summary, PN G069.7–00.0 has distance between  $11.1 \pm 0.6$  kpc and  $12.0 \pm 0.7$  kpc, which is much larger than previous distances, e.g., 3.31 kpc by (Cahn et al. 1992), 3.26 kpc by Zhang (1995), 4.23 kpc by Stanghellini et al. (2008), 3.09 kpc by van de Steene & Zijlstra (1995) and 2.96 kpc by Phillips (2004). So we prefer to keep an open question for its distance.

PN G070.7+01.2 (Fig. 9):

Based on the observed tangent point velocity of 22 km  $s^{-1}$  in the PN spectrum, we take a rotational velocity  $V_R = 230$  km  $s^{-1}$  at the tangent point in the direction  $l = 70.7^\circ$ . The fact that the H I absorption features of the PN and three background sources appear at the tangent point velocity implies all sources are beyond the tangent point. So we obtain a lower limit distance of  $2.5 \pm 1.6$  kpc for the PN. There are clear absorption features at negative velocities in nearby sources spectra, while no absorption feature is detected at these velocities in the PN spectrum. This implies the PN is within solar circle ( $5.0 \pm 0.7$  kpc). So PN G070.7+01.2 is between  $2.5 \pm 1.6$  kpc and  $5.0 \pm 0.7$  kpc.

Bally et al. (1989) have given a distance of  $4.5 \pm 1.0$  kpc using the line width of CO emission and angular radius of CO cloud. Therefore, the upper distance of  $5.0 \pm 0.7$  kpc is suitable for the PN.

PN G084.9–03.4 (Fig. 10):

Fig. 10 shows the tangent point velocity (18 km  $s^{-1}$ ) towards the PN, which is larger than the expected value (0.8 km  $s^{-1}$ ). We obtain the rotation velocity  $V_R = 237$  km  $s^{-1}$  at the tangent point in the direction  $l = 84.9^\circ$ . The H I spectra of the PN and two background sources show

clear H I absorption features from  $\sim 0$  km  $s^{-1}$  up to the tangent point (18 km  $s^{-1}$ ), hinting the PN and two background sources are beyond the tangent point. So we obtain the lower limit distance of  $\sim 0.7$  kpc for this PN. The prominent H I emission at  $-20$  km  $s^{-1}$  appears in the spectra of the PN as well as two nearby background sources, whereas its respective absorption feature is detected only in two background sources. This gives an upper limit distance of  $4.3 \pm 0.6$  kpc for the PN. Hence, the distance of the PN is between  $\sim 0.7$  kpc and  $4.3 \pm 0.6$  kpc.

This PN, named NGC 7027 as the most luminous Galactic PN, has a distance measured by various methods, such as statistical distances (0.7 kpc, Maciel (1984); 0.63 kpc, van de Steene & Zijlstra (1995); 0.64 kpc, Zhang (1995)), reddening ( $< 1.15$  kpc, Navarro et al. 2012), expansion parallax ( $0.703 \pm 0.095$  kpc, Hajian et al. (1993);  $0.98 \pm 1.0$  kpc, Zijlstra et al. (2008);  $0.88 \pm 0.15$  kpc, Mason (1989);  $0.68 \pm 0.17$  kpc, Mellema (2004)). In fact, Pottasch et al. (1982) gave a upper limit distance 4.5 kpc also measured by comparing the H I absorption feature at  $-20$  km  $s^{-1}$  between the PN and a background source. So the lower limit distance 0.7 kpc is reliable for PN G084.9–03.4.

PN G089.0+00.3 (Fig. 11):

The disagreement between the observed tangent point velocity (10 km  $s^{-1}$ ) shown in Fig. 11 and the expected value (0.03 km  $s^{-1}$ ) may be due to random motions of H I clouds at the tangent point in the direction  $l = 89^\circ$ . Fig. 11 shows H I spectra of the PN and background sources. The absorption features at  $-70$  km  $s^{-1}$  and  $-40$  km  $s^{-1}$  are likely not real, and two significant absorption features at  $-20$  km  $s^{-1}$  and  $\sim 0$  km  $s^{-1}$  indicate that a reliable lower limit distance for this PN is  $3.5 \pm 0.6$  kpc. No reliable upper limit distance can be determined for this PN.

The distance of this PN (also named NGC 7026) has been investigated previously by using H I absorption ( $2.5 \pm 1.0$  kpc, Gathier et al. 1986a), statistical method (e.g., 2.35 kpc, Stanghellini et al. (2008); 2.03 kpc, Zhang (1995)), reddening (e.g.,  $1.57 \pm 0.65$  kpc, Kaler & Lutz (1985); 2.3 kpc, Pottasch (1983)), surface gravity method (e.g., 3.5 kpc, Zhang (1993); 4.2 kpc, Cazetta & Maciel (2000)), spectroscopic method (1.9 kpc, Gruendl et al. 2004). Our result is reasonably consistent with surface gravity distance and larger than others. Actually, Gathier et al. (1986a) found a weak absorption at  $\sim -20$  km  $s^{-1}$  in the PN spectrum, but they did not take this absorption as clear evidence to constrain its distance. The  $-7$  km  $s^{-1}$  absorption feature they chose for the lower limit distance of  $2.5 \pm 1.0$  kpc is also detected in our data. Since our data has higher resolution and more sensitive than before, the absorption at  $-20$  km  $s^{-1}$  detected in our work can be used to determine a more reliable lower limit distance of  $3.5 \pm 0.6$  kpc for this PN.

PN G107.8+02.3 (Fig. 12):

The absorption features at positive velocity in both the PN and G108.7+02.57 are partly due to a cloud with anomalous motion. Clear absorption features are present at  $\sim -30$  km  $s^{-1}$ ,  $\sim -60$  km  $s^{-1}$  and  $\sim -105$  km  $s^{-1}$  in the spectrum of background source G108.7+02.57, while no absorption features are detected at the velocities in

the PN spectrum. This implies the PN is in front of the H I cloud at  $\sim -30 \text{ km s}^{-1}$ , i.e.,  $2.8 \pm 0.5 \text{ kpc}$ . The CO emission, H I emission and absorption features at  $-12 \text{ km s}^{-1}$  in the PN spectrum indicate a lower limit distance of  $1.2 \pm 0.6 \text{ kpc}$ . Therefore, the distance of PN G107.8+02.3 is between  $1.2 \pm 0.6 \text{ kpc}$  and  $2.8 \pm 0.5 \text{ kpc}$ .

For this PN, also named NGC 7354, the distance has been measured by various methods. Gathier et al. (1986a) suggested a H I absorption distance  $1.5 \pm 0.5$  determined by the nearby H II regions of the PN. Giammanco et al. (2011) obtained a distance of  $1.0 \pm 0.15 \text{ kpc}$  based on the distance-extinction relationship in the direction toward the PN. Zhang (1993) gave a distance of  $2.1 \text{ kpc}$  by the surface gravity method. The revised Shklovshy method suggested distances of  $1.27 \text{ kpc}$  by Cahn et al. (1992),  $1.3 \text{ kpc}$  by Zhang (1995),  $1.23 \text{ kpc}$  by van de Steene & Zijlstra (1995),  $1.19 \text{ kpc}$  by Phillips (2004), and  $1.70 \text{ kpc}$  by Stanghellini et al. (2008). So the lower distance of  $1.2 \pm 0.6 \text{ kpc}$  seems reasonable for the PN.

PN G138.8+02.8 (Fig. 13):

There are clear H I absorption and CO emission features at  $-42 \text{ km s}^{-1}$  in the direction of G138.8+02.14, while similar absorption is not detected in the PN spectrum. This indicates that the PN is in front of the H I cloud at  $-42 \text{ km s}^{-1}$ . The PN spectrum reveals one reliable H I absorption feature at  $-20 \text{ km s}^{-1}$ . Therefore, we obtain a lower limit distance of  $1.6 \pm 0.5 \text{ kpc}$  and an upper limit distance of  $3.8 \pm 0.8 \text{ kpc}$ .

PN G138.8+02.8 (also named IC 289) has statistical distances of  $1.43 \text{ kpc}$  by Cahn et al. (1992),  $1.68 \text{ kpc}$  by Zhang (1995),  $1.45 \text{ kpc}$  by Stanghellini et al. (2008),  $1.18 \text{ kpc}$  by Phillips (2004), and  $1.48 \text{ kpc}$  by van de Steene & Zijlstra (1995); as well as a reddening distance of  $2.71 \pm 0.195 \text{ kpc}$  (Kaler & Lutz 1985). So we suggest a distance of  $1.6 \pm 0.5 \text{ kpc}$  for the PN.

PN G147.4-02.3 (Fig. 14):

Both H I emission and absorption features at  $-35 \text{ km s}^{-1}$  appear in the spectra of the PN as well as its nearby background sources. This implies that the PN is behind the H I cloud at  $3.6 \pm 0.9 \text{ kpc}$ . In addition, the presence of clear H I emission and the absence of absorption at  $-60 \text{ km s}^{-1}$  in the PN spectrum indicates that the PN is in front of the H I cloud at  $8.7 \pm 1.7 \text{ kpc}$ . Overall, the distance of the PN is between  $3.6 \pm 0.9 \text{ kpc}$  and  $8.7 \pm 1.7 \text{ kpc}$ .

The distance of the PN was measured by several methods previously, i.e., surface gravity distance of  $2.2-3.1 \text{ kpc}$  by Cazetta & Maciel (2001), the revised Shklovsky distances of  $3.39 \text{ kpc}$  by Phillips (2004) and  $3.53 \text{ kpc}$  by Zhang (1995), as well as a reddening distance of  $3.3 \pm 0.35 \text{ kpc}$  by Giammanco et al. (2011). These are consistent with our lower limit distance  $3.6 \pm 0.9 \text{ kpc}$ .

PN G169.7-00.1 (Fig. 15):

This PN is most likely a H II region as suggested by Zijlstra et al. (1990), which is close to the Galactic plane (see Fig. 15). The H I emission and absorption features at  $-32 \text{ km s}^{-1}$  in spectra of the PN and the background sources imply they are beyond the H I cloud at  $\sim 14.7 \text{ kpc}$ , see Fig. 1 (upper-right panel). This lower limit distance is derived by considering the average random velocity

$6 \text{ km s}^{-1}$  of H I clouds. No upper limit distance can be derived. Our lower limit is much larger than previous measurements, i.e.,  $1.37 \text{ kpc}$  by Cahn et al. (1992),  $1.86 \text{ kpc}$  by Zhang (1995),  $1.26 \text{ kpc}$  by Phillips (2004),  $1.39 \text{ kpc}$  by Stanghellini et al. (2008). So we prefer to keep an open question for its distance.

PN G259.1+00.9 (Fig. 16):

There is strong continuous H I emission and absorption between  $0$  to  $12 \text{ km s}^{-1}$  in the PN spectrum (Fig. 16), but no absorption features appear up to the tangent point velocity after  $12 \text{ km s}^{-1}$  ( $3\sigma=0.27$ ). This means that the PN is beyond the near side for  $12 \text{ km s}^{-1}$ , i.e.,  $1.6 \pm 0.6 \text{ kpc}$ . Unlike the PN spectrum, the two background sources show absorption features at velocities of  $20 \text{ km s}^{-1}$  and  $40 \text{ km s}^{-1}$ . This implies that the PN is in front of the H I at  $20 \text{ km s}^{-1}$ , i.e.,  $2.4 \pm 0.6 \text{ kpc}$ . So the distance of the PN is between  $1.6 \pm 0.6 \text{ kpc}$  and  $2.4 \pm 0.6 \text{ kpc}$ . In comparison with previous work obtained by statistical method ( $0.9 \text{ kpc}$ , Cahn et al. (1992);  $1.07 \text{ kpc}$ , Zhang (1995)) and Spectroscopic distance ( $0.7 \text{ kpc}$ , Jones et al. 2014). We suggest a distance of  $1.6 \pm 0.6 \text{ kpc}$  for this PN.

PN G333.9+00.6 (Fig. 17):

Fig. 17 shows this PN has a poor absorption spectrum. One possible absorption feature at  $-26 \text{ km s}^{-1}$  can be used to provide a lower limit distance  $1.9 \pm 0.4 \text{ kpc}$ . No upper limit distance can be derived for the PN. In fact, the previous spectroscopic distance ( $1.0-1.5 \text{ kpc}$ ) obtained by Morgan et al. (2003) agrees with our result. This PN likely has a distance of  $1.9 \pm 0.4 \text{ kpc}$ .

PN G352.6+00.1 (Fig. 18):

Two background sources (G352.5-0.17, G351.6+0.17) show reliable absorption features at the tangent point velocity, while this does not appear in the PN spectrum. This implies that the PN is in front of the tangent point. There appear H I emission and absorption at  $-20 \text{ km s}^{-1}$  in the spectra of the PN and H II region G353.4-00.3. In fact the PN is behind the H II region G353.4-00.3 ( $3.2 \pm 0.8 \text{ kpc}$ , Tian et al. (2008)). In addition, an absorption feature at  $-50 \text{ km s}^{-1}$  is seen in the spectrum of G351.6+0.17, while H I emission is seen but no absorption at the same velocity in the PN spectrum. This implies the PN is in front of near distance of  $-50 \text{ km s}^{-1}$ , i.e.,  $5.0 \pm 0.3 \text{ kpc}$ . So PN G352.6+00.1 is between  $3.2 \pm 0.8 \text{ kpc}$  and  $5.0 \pm 0.3 \text{ kpc}$ .

Maciel (1984) gave a lower limit  $0.9 \text{ kpc}$  for this PN by assuming a relationship between the nebular ionized mass and radius. Zhang (1995) and van de Steene & Zijlstra (1995) suggested distances of  $1.40 \text{ kpc}$  and  $1.37 \text{ kpc}$  based on the revised relation between radio surface brightness temperature and nebula radius. Therefore, we adopt  $3.2 \pm 0.8 \text{ kpc}$  for the PN.

PN G352.8-00.2 (Fig. 19):

The weak absorption features at the tangent velocity,  $-36 \text{ km s}^{-1}$ , and  $-90 \text{ km s}^{-1}$  in the H I spectrum of PN G352.8-00.2 have a S/N of about  $3\sigma$  ( $0.24$ ), so we do not regard it as real absorption. The absorption feature at  $-20 \text{ km s}^{-1}$  is detected in the spectra of three background sources, but does not appear in the PN spectrum, implying the PN is in front of H I ( $3.2 \pm 0.8 \text{ kpc}$ , Tian et al.

2008). In addition, the presence of clear H I emission and absence of absorption feature at  $-10 \text{ km s}^{-1}$  in the PN spectrum reveals an lower limit distance of  $2.1 \pm 0.9 \text{ kpc}$  for the PN. We conclude that the distance of the PN is between  $2.1 \pm 0.9 \text{ kpc}$  and  $3.2 \pm 0.8 \text{ kpc}$ .

The distance of the PN was also suggested by statistical methods (e.g.  $0.8 \text{ kpc}$ , Maciel (1984);  $1.36 \text{ kpc}$ , Phillips (2004);  $1.53 \text{ kpc}$ , Cahn et al. (1992);  $1.39 \text{ kpc}$ , Zhang (1995);  $1.34 \text{ kpc}$ , van de Steene & Zijlstra (1995)). Hence, we prefer the distance of  $2.1 \pm 0.9 \text{ kpc}$  for the PN.

#### 4. SUMMARY

We analyze the H I absorption spectra of 18 Galactic plane PNe and estimate their kinematic distances in this paper. The final results are shown in Table 2. We compare new kinematic distances of 15 PNe with the previous results determined from other methods, such as surface gravity (5 PNe, e.g. Zhang 1993; Cazetta & Maciel 2000), expansion parallax (1 PN, e.g. Hajian et al. 1993; Zijlstra et al. 2008), reddening (5 PNe, e.g. Kaler & Lutz 1985; Giammanco et al. 2011), statistical (13 PNe, e.g. Cahn et al. 1992; Zhang 1995), H I absorption (4 PNe, e.g. Bally et al. 1989; Gathier et al. 1986a). By considering the additional distance information, we determine distances for 13 PNe with uncertainties ranging from 10% to 50%. For 8 out of 13 PNe, the kinematic distances are determined with uncertainties less than 25%. For three objects (PN G020.9–01.1, PN G029.0+00.4, PN G084.9–03.4) the kinematic distances are derived with uncertainties less than 10%, and for the other ten cases the kinematic distances are estimated with uncertainties less than 50%. This is a significant improvement compared against most of the previous measurements with uncertainties of two or three factor smaller. For three cases the kinematic distance are derived with lower and upper distance limits (see Table 2). We do not suggest distances for PN G069.7–00.0 and PN G169.7–00.1 based on our current H I measurements only. For PN candidate PN G030.2–00.1, which was discussed by Anderson et al. (2011), its luminosity is  $\sim 225$  times stronger

than the most luminous Galactic PN NGC 7027 ( $506 \text{ mJy}$  at  $\sim 8.6 \text{ GHz}$ , see Zijlstra et al. 2008), so G030.2–00.1 might not be a PN.

In addition, our spectra have revealed that five of the PNe show larger tangent point velocities than expected from the rotation curve model when adopting IAU value of  $V_0 = 220 \text{ km s}^{-1}$ . Three of them are located near  $53^\circ$ . This is consistent with the previous studies in Levine et al. (2008) and Leahy et al. (2008).

We compare our distances with the previous measurements based on the data in table 2 (also see Fig. 20). We find that all other work (except statistical results, see Fig. 20, left panel) show obvious dispersion between each other, and that our distance measurements are well consistent with the most reliable method, i.e. expansion parallax. Our distance measurements are consistent with Frew et al. (2016) when considering the uncertainties, but larger than the other statistical results (see Fig. 20, middle and right panels). In order to investigate the possible effects of some PNe parameters on our measurements, we have tried to find the correlation between these parameters (e.g., radius, reddening) and the residuals which obtained by subtracting our distances from those obtained by other methods. No obvious correlation is found. A total number of 22 PNe have H I absorption measurements in the literatures. Our work significantly increases the number of Galactic PNe with H I absorption measurements and known kinematic distances.

We acknowledge support from the NSFC (11473038, 11273025, 1126114046) and also support from China's Ministry of Science and Technology under the State Key Development Program for Basic Research (2012CB821800, 2013CB837901). D. A. Leahy is supported by a grant from the Natural Sciences and Engineering Research Council of Canada. The work has made use of data from the International Galactic Plane Survey (<http://www.ras.ualgary.ca/IGPS/>).

#### REFERENCES

- Anantharamaiah, K. R., Radhakrishnan, V., & Shaver, P. A. 1984, *A&A*, 138, 131  
 Anderson, L. D., Bania, T. M., Balser, D. S., & Rood, R. T. 2011, *ApJS*, 194, 32  
 Bally, J., Pound, M. W., Stark, A. A., et al. 1989, *ApJ*, 338, L65  
 Bojčić, I. S., Parker, Q. A., Filipović, M. D., & Frew, D. J. 2011, *MNRAS*, 412, 223  
 Bovy, J., Allende Prieto, C., Beers, T. C., et al. 2012, *ApJ*, 759, 131  
 Cahn, J. H., Kaler, J. B., & Stanghellini, L. 1992, *A&AS*, 94, 399  
 Cazetta, J. O., & Maciel, W. J. 2000, *RMxAA*, 36, 3  
 —. 2001, *Ap&SS*, 277, 393  
 Ciardullo, R., Bond, H. E., Sipior, M. S., et al. 1999, *AJ*, 118, 488  
 Condon, J. J., & Kaplan, D. L. 1998, *ApJS*, 117, 361  
 Crovisier, J. 1978, *A&A*, 70, 43  
 Dickey, J. M., & Lockman, F. J. 1990, *ARA&A*, 28, 215  
 Dobbs, C. L., Bonnell, I. A., & Pringle, J. E. 2006, *MNRAS*, 371, 1663  
 Eisenhauer, F., Genzel, R., Alexander, T., et al. 2005, *ApJ*, 628, 246  
 Frew, D. J., Parker, Q. A., & Bojčić, I. S. 2016, *MNRAS*, 455, 1459  
 Gathier, R., Pottasch, S. R., & Goss, W. M. 1986a, *A&A*, 157, 191  
 Gathier, R., Pottasch, S. R., & Pel, J. W. 1986b, *A&A*, 157, 171  
 Giammanco, C., Sale, S. E., Corradi, R. L. M., et al. 2011, *A&A*, 525, A58  
 Gruendl, R. A., Chu, Y.-H., Guerrero, M. A., & Meixner, M. 2004, in *Bulletin of the American Astronomical Society*, Vol. 36, American Astronomical Society Meeting Abstracts, 138.05  
 Hajian, A. R., Terzian, Y., & Bignell, C. 1993, *AJ*, 106, 1965  
 Harris, H. C., Dahn, C. C., Canzian, B., et al. 2007, *AJ*, 133, 631  
 Heyer, M. H., & Terebey, S. 1998, *ApJ*, 502, 265  
 Jackson, J. M., Rathborne, J. M., Shah, R. Y., et al. 2006, *ApJS*, 163, 145  
 Jacoby, G. H., Morse, J. A., Fullton, L. K., Kwitter, K. B., & Henry, R. B. C. 1997, *AJ*, 114, 2611  
 Jones, D., Boffin, H. M. J., Miszalski, B., et al. 2014, *A&A*, 562, A89  
 Kaler, J. B., & Lutz, J. H. 1985, *PASP*, 97, 700  
 Kwitter, K. B., Méndez, R. H., Peña, M., et al. 2014, *RMxAA*, 50, 203  
 Leahy, D. A., & Tian, W. W. 2008, *AJ*, 135, 167  
 Leahy, D. A., & Tian, W. W. 2010, in *Astronomical Society of the Pacific Conference Series*, Vol. 438, *The Dynamic Interstellar Medium: A Celebration of the Canadian Galactic Plane Survey*, ed. R. Kothés, T. L. Landecker, & A. G. Willis, 365  
 Leahy, D. A., Tian, W. W., & Wang, Q. D. 2008, *AJ*, 136, 1477  
 Levine, E. S., Heiles, C., & Blitz, L. 2008, *ApJ*, 679, 1288  
 Luo, S. G., Condon, J. J., & Yin, Q. F. 2005, *ApJS*, 159, 282  
 Maciel, W. J. 1984, *A&AS*, 55, 253  
 Masson, C. R. 1986, *ApJ*, 302, L27  
 —. 1989, *ApJ*, 336, 294  
 McClure-Griffiths, N. M., Dickey, J. M., Gaensler, B. M., et al. 2005, *ApJS*, 158, 178  
 Mellema, G. 2004, *A&A*, 416, 623

TABLE 2  
FINAL KINEMATIC DISTANCES OF PLANETARY NEBULAE

PN G Name	PN Name	Distance limits kpc	Final distance kpc	Distance by others(Ref.) kpc	Method
G020.9−01.1	M 1−51	3.1±0.3−7.1±0.6	3.1±0.3	2.4(C01) 1.75(C92),1.66(S95) 1.74(Z95),2.29(S08) 1.59(Ph04) 2.31±0.75(F16)	surface gravity statistical statistical statistical statistical
G029.0+00.4	A66 48	3.5±0.3−6.6±1.0	3.5±0.3	1.2(M84) 1.41±0.43(F16)	statistical statistical
G030.2−00.1	-	10.9±0.3−13.2±0.5	10.9±0.3−13.2±0.5	-	-
G051.5+00.2	KLW 1	4.7±1.4−9.5±0.4	4.7±1.4−9.5±0.4	-	-
G052.1+01.0	-	4.7±1.4−5.4±0.7	4.7±1.4−5.6±0.8	-	-
G055.5−00.5	M 1−71	4.3±1.5−8.6±0.4	4.3±1.5	1.66(C92),3.68(S08) 3.17(Z95),3.17(S95) 2.88±0.91(F16) 2.9±0.4(G11)	statistical statistical statistical reddening
G069.7−00.0	K 3−55	11.07±0.61−12.02±0.67	?	3.31(C92),4.23(S08) 3.26(Z95),3.09(S95) 2.96(Ph04) 3.54±1.32(F16)	statistical statistical statistical statistical
G070.7+01.2	M 3−60	2.5±1.6−5.0±0.7	5.0±0.7	4.5±1.0(B89)	H I absorption
G084.9−03.4	NGC 7027	0.7−4.3±0.6	0.7	0.7(M84),0.64(Z95) 0.27(C92),0.63(S95) 0.94±0.27(F16) 2.3−2.9(C01) 0.703±0.095(H93) 0.98±1.0(Z08) 0.94±0.2(M86) 0.88±0.15(M89) 0.68±0.17(M04) <1.15(N12) <4.5(P82)	statistical statistical statistical surface gravity expansion parallax expansion parallax expansion parallax expansion parallax expansion parallax reddening H I absorption
G089.0+00.3	NGC 7026	≥3.5±0.6	3.5±0.6	2.5±1.0(G86) 1.9(C92),2.35(S08) 2.03(Z95),1.91(Ph04) 1.94(S95) 1.67±0.48(F16) 1.57±0.65(K85) 2.3(P83),<1.5(G11) 3.5(Z93),4.2(C00) 1.9(G04) 1.5±0.5(G86) 1.27(C92),1.19(Ph04)	H I absorption statistical statistical statistical statistical reddening reddening surface gravity Spectroscopic parallax H I absorption statistical
G107.8+02.3	NGC 7354	1.2±0.6−2.8±0.5	1.2±0.6	1.3(Z95),1.70(S08) 1.23(S95) 1.26±0.37(F16) 1.0±0.15(G11) 3.43±0.62(K85) 2.1(Z93),3.2(C00)	statistical statistical statistical reddening reddening surface gravity
G138.8+02.8	IC 289	1.6±0.6−3.8±0.6	1.6±0.6	2.71±0.195(K85) 1.43(C92),1.45(S08) 1.68(Z95),1.18(Ph04) 1.48(S95) 1.88±0.58(F16)	reddening statistical statistical statistical statistical
G147.4−02.3	M 1−4	3.6±0.9−8.7±1.7	3.6±0.9	2.2−3.1(C01) 2.99(C92),3.36(S95) 3.53(Z95),3.39(Ph04) 6.6(S08) 5.18±1.55(F16) 3.3±0.35(G11)	surface gravity statistical statistical statistical statistical reddening
G169.7−00.1	IC 2120	≥14.7	?	1.37(C92),1.388(S08) 1.86(Z95),1.26(Ph04)	statistical statistical
G259.1+00.9	Hen 2−11	1.6±0.6−2.4±0.6	1.6±0.6	0.9(C92),1.07(Z95) 0.80±0.24(F16) 0.7(J14)	statistical statistical Spectroscopic
G333.9+00.6	PMR 5	≥1.9±0.4	1.9±0.4	1.0−1.5(M03)	Spectroscopic
G352.6+00.1	H 1−12	3.2±0.8−5.0±0.3	3.2±0.8	>0.9(M84) 1.40(Z95),1.37(S95) 2.42±0.84(F16)	statistical statistical statistical
G352.8−00.2	H 1−13	2.1±0.9−3.2±0.8	2.1±0.9	0.8(M84),1.36(Ph04) 1.53(C92),1.39(Z95) 1.34(S95) 1.74±0.59(F16)	statistical statistical statistical statistical

Ref.: C01- Cazetta & Maciel (2001), C92-Cahn et al. (1992), S95-van de Steene & Zijlstra (1995), Z95-Zhang (1995)  
S08-Stanghellini et al. (2008), B89-Bally et al. (1989), N12-Navarro et al. (2012), G11-Giammanco et al. (2011)  
K85-Kaler & Lutz (1985), G86-Gathier et al. (1986a), C00-Cazetta & Maciel (2000), G04-Gruendl et al. (2004)  
P83-Pottasch (1983), Z08-Zijlstra et al. (2008), H93-Hajian et al. (1993), M84-Maciel (1984), Z93-Zhang (1993)  
Ph04-Phillips (2004), M04-Mellema (2004), M86-Masson (1986), M03-Morgan et al. (2003), M89-Masson (1989)  
J14-Jones et al. (2014), P82-Pottasch et al. (1982), F16-Frew et al. (2016)  
?-represent that we keep an open question for its distance.



- Mendez, R. H., Kudritzki, R. P., Herrero, A., Husfeld, D., & Groth, H. G. 1988, *A&A*, 190, 113
- Morgan, D. H., Parker, Q. A., & Cohen, M. 2003, *MNRAS*, 346, 719
- Napiwotzki, R., & Schoenberner, D. 1995, *A&A*, 301, 545
- Navarro, S. G., Corradi, R. L. M., & Mampaso, A. 2012, in *IAU Symposium*, Vol. 283, *IAU Symposium*, 460–461
- Phillips, J. P. 2004, *MNRAS*, 353, 589
- Pottasch, S. R. 1983, in *IAU Symposium*, Vol. 103, *Planetary Nebulae*, ed. D. R. Flower, 391–407
- Pottasch, S. R., Goss, W. M., Gathier, R., & Arnal, E. M. 1982, *A&A*, 106, 229
- Reid, M. J., Brunthaler, A., Menten, K. M., et al. 2007, in *IAU Symposium*, ed. J. M. Chapman & W. A. Baan, Vol. 242, 348–355
- Reid, M. J., Menten, K. M., Zheng, X. W., et al. 2009, *ApJ*, 700, 137
- Shaver, P. A., Radhakrishnan, V., Anantharamaiah, K. R., et al. 1982, *A&A*, 106, 105
- Shklovskii, I. S. 1956, *Kosmicheskoe radiolzluchenie*.
- Stanghellini, L., Shaw, R. A., & Villaver, E. 2008, *ApJ*, 689, 194
- Stil, J. M., Taylor, A. R., Dickey, J. M., et al. 2006, *AJ*, 132, 1158
- Taylor, A. R., Gibson, S. J., Peracaula, M., et al. 2003, *AJ*, 125, 3145
- Terzian, Y. 1997, in *IAU Symposium*, Vol. 180, *Planetary Nebulae*, ed. H. J. Habing & H. J. G. L. M. Lamers, 29
- Tian, W. W., & Leahy, D. A. 2008, *MNRAS*, 391, L54
- Tian, W. W., Leahy, D. A., Haverkorn, M., & Jiang, B. 2008, *ApJ*, 679, L85
- Tian, W. W., Leahy, D. A., & Li, D. 2010, *MNRAS*, 404, L1
- Tian, W. W., Leahy, D. A., & Wang, Q. D. 2007, *A&A*, 474, 541
- van de Steene, G. C., & Zijlstra, A. A. 1995, *A&A*, 293, 541
- Viironen, K., Greimel, R., Corradi, R. L. M., et al. 2009, *A&A*, 504, 291
- Zhang, C. Y. 1993, *ApJ*, 410, 239
- . 1995, *ApJS*, 98, 659
- Zhu, H., Tian, W. W., Torres, D. F., Pedalletti, G., & Su, H. Q. 2013, *ApJ*, 775, 95
- Zijlstra, A., Pottasch, S., & Bignell, C. 1990, *A&AS*, 82, 273
- Zijlstra, A. A., van Hoof, P. A. M., & Perley, R. A. 2008, *ApJ*, 681, 1296

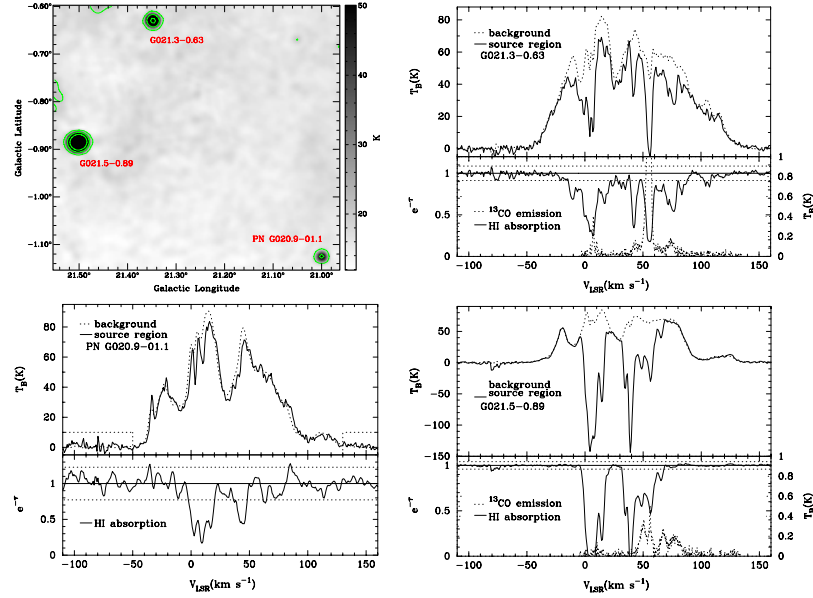


FIG. 2.— 1420 MHz continuum image of PN G020.9–01.1 and its background sources (top left), and the H I spectra of PN G020.9–01.1 (bottom left), G021.3–0.63 (top right) and G021.5–0.89 (bottom right). The map has superimposed contours (20,50,130 K) of 1420 MHz continuum emission. The dotted horizontal lines in the lower panel of the PN spectrum show the  $3\sigma$  noise level. This description applies for all the spectra of PNe and background sources from Fig. 2 to Fig. 19.

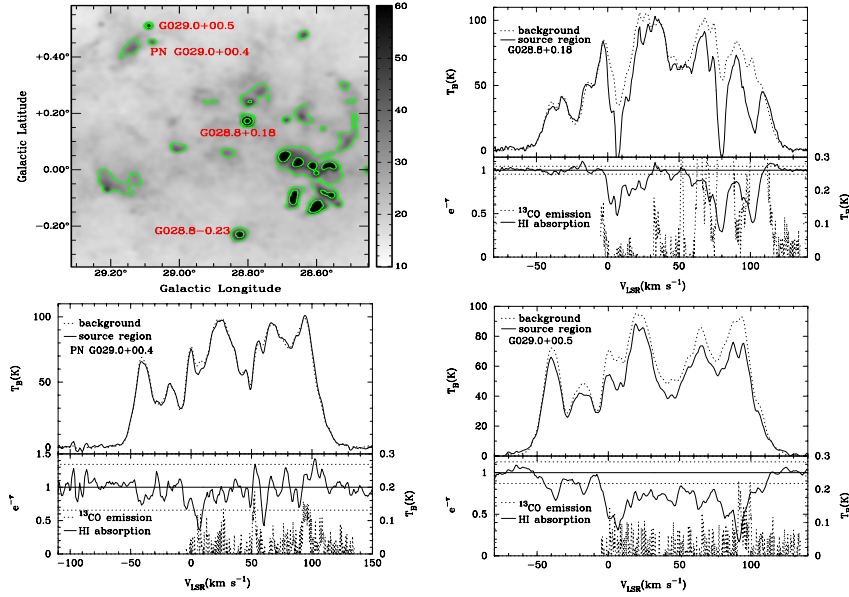


FIG. 3.— 1420 MHz continuum image of PN G029.0+00.4, and its background sources (top left), and the H I spectra of PN G029.0+00.4 (bottom left), G028.8+0.18 (top right), and G029.0+00.5 (bottom right). The H I spectra of G028.8–0.23 is listed in appendix Fig. 21. The map has superimposed contours (30,50,120 K) of 1420 MHz continuum emission.

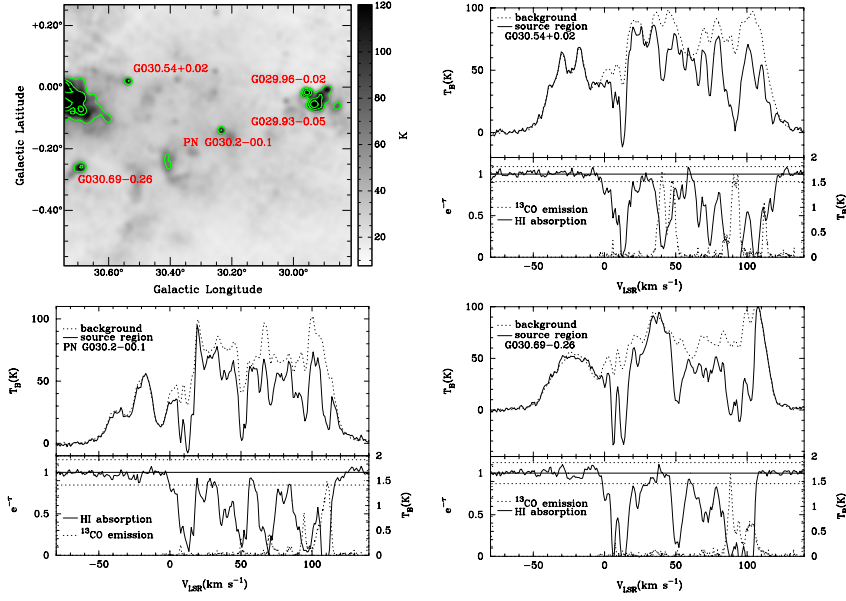


FIG. 4.— 1420 MHz continuum image of PN G030.2–00.1 and its nearby background source (top left), and the H I spectra of PN G030.2–00.1 (bottom left), G030.54+0.02 (top right), and G030.69–0.26 (bottom right). The H I spectra of G029.93–0.05 and G029.96–0.02 are listed in appendix Fig. 21. The map has superimposed contours (65,125,230 K) of 1420 MHz continuum emission.

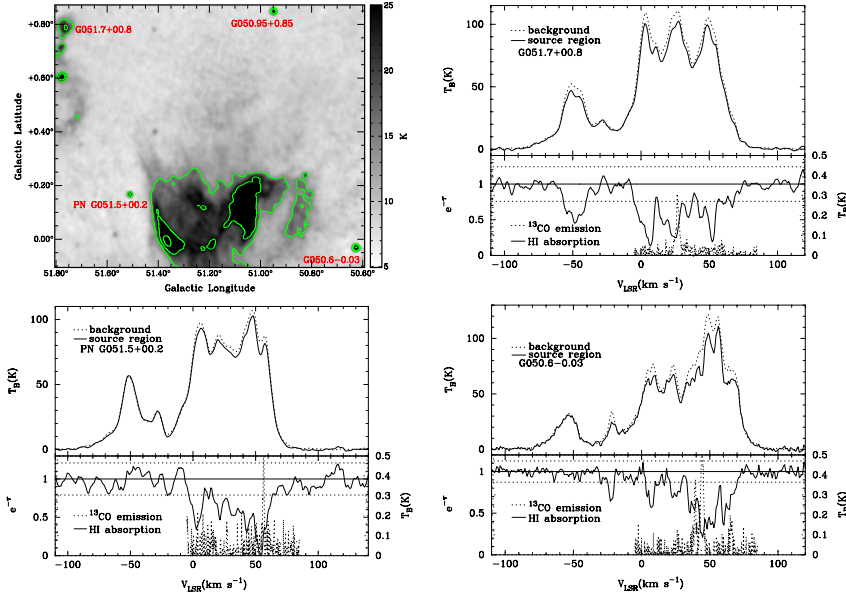


FIG. 5.— 1420 MHz continuum image of PN G051.5+00.2 and its nearby background sources (top left), and the H I spectra of PN G051.5+00.2 (bottom left), G051.7+00.8 (top right), and G050.6–0.03 (bottom right). The H I spectra of G050.95+0.85 is shown in appendix Fig. 21. The map has superimposed contours (15,25,60 K) of 1420 MHz continuum emission.

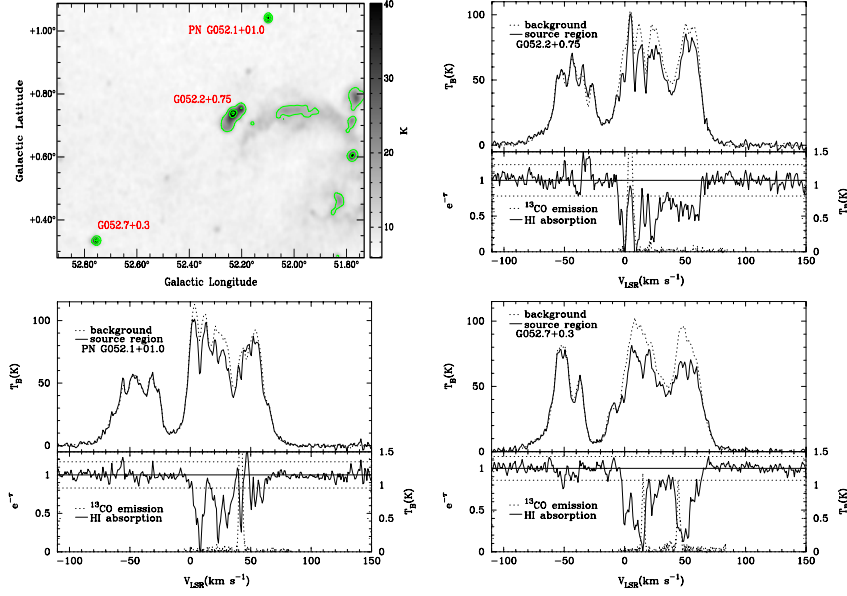


FIG. 6.— 1420 MHz continuum image of PN G052.1+01.0, and its background sources (top left), and the H I spectra of PN G052.1+01.0 (bottom left), G052.2+0.75 (top right) and G052.7+0.3 (bottom right). The map has superimposed contours (15,35,55 K) of 1420 MHz continuum emission.

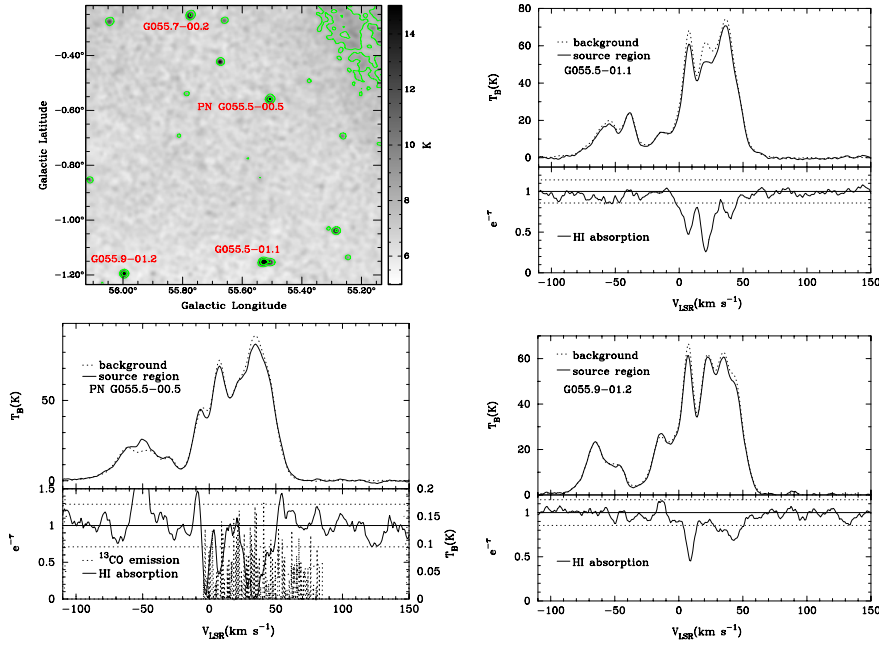


FIG. 7.— 1420 MHz continuum image of PN G055.5-00.5 and its nearby background sources (top left), and the H I spectra of PN G055.5-00.5 (bottom left), G055.5-01.1 (top right), and G055.9-01.2 (middle right). The H I spectra of G055.7-00.2 is shown in appendix Fig. 21. The map has superimposed contours (8,15,35 K) of 1420 MHz continuum emission.

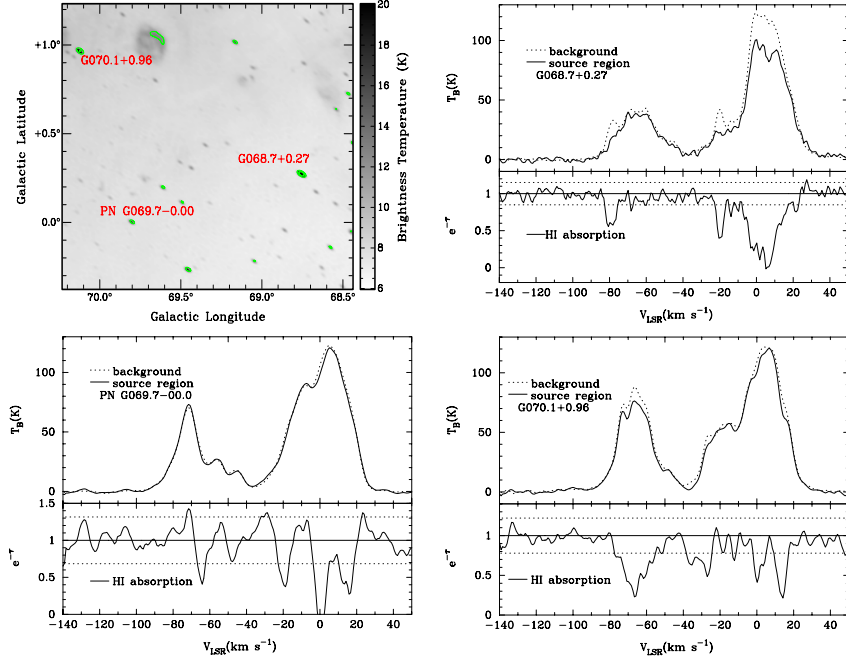


FIG. 8.— 1420 MHz continuum image of PN G069.7-00.0, and its nearby background sources (top left), and the H I spectra of PN G069.7-00.0 (bottom left), G068.7+0.27 (top right) and G070.1+0.96 (bottom right). The map has superimposed contours (5,12,32 K) of 1420 MHz continuum emission.

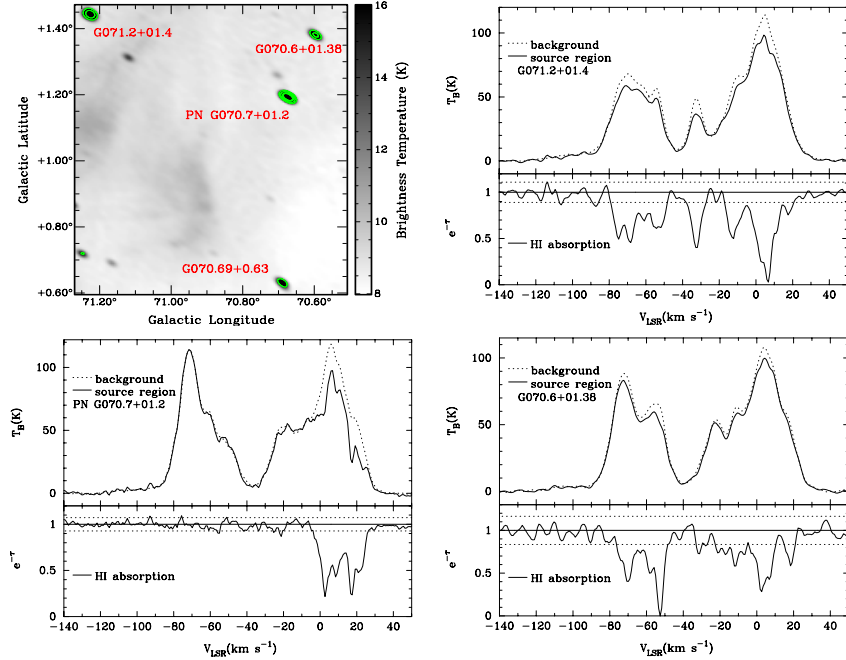


FIG. 9.— 1420 MHz continuum image of PN G070.7+01.2, and its background sources (top left), and the H I spectra of PN G070.7+01.2 (bottom left), G071.2+01.4 (top right), and G070.6+01.38 (bottom right). The H I spectra of G070.69+0.63 is listed in appendix Fig. 21. The map has superimposed contours (15,25,50 K) of 1420 MHz continuum emission.

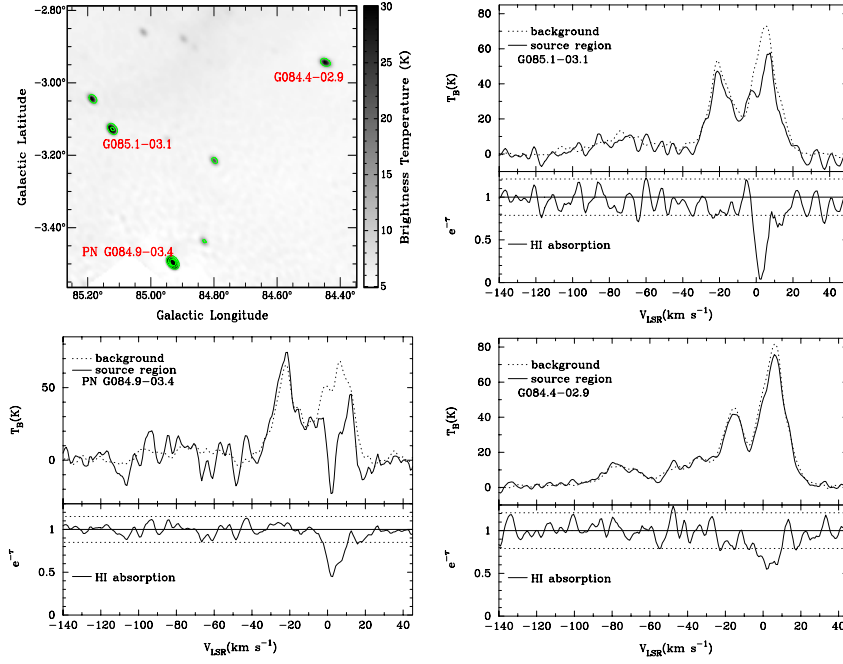


FIG. 10.— 1420 MHz continuum image of PN G084.9–03.4 and it nearby background sources (top left), and the H I spectra of PN G084.9–03.4 (bottom left), G085.1–03.1 (top right), G084.4–02.9 (bottom right). The map has superimposed contours (15,50,100 K) of 1420 MHz continuum emission.

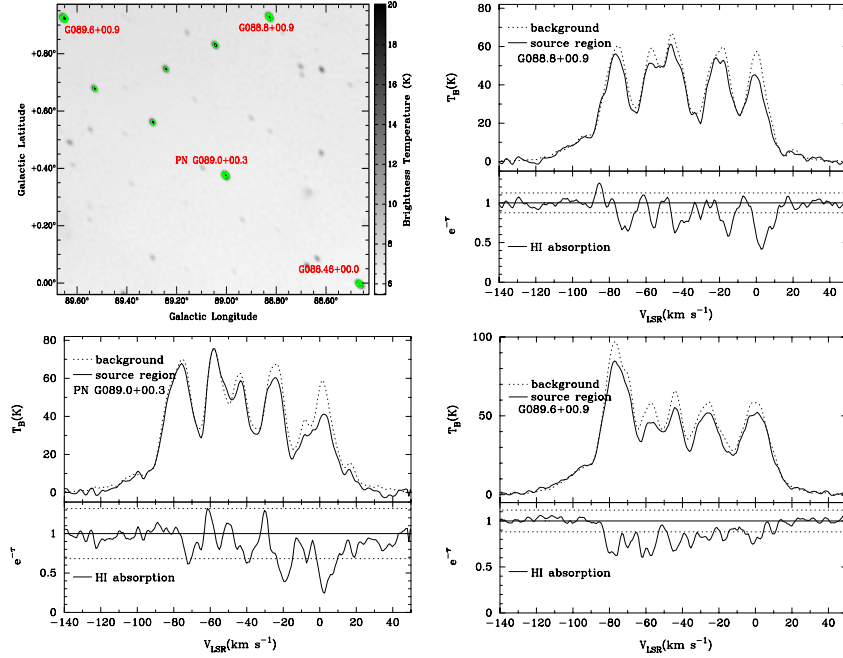


FIG. 11.— 1420 MHz continuum image of PN G089.0+00.3 and its nearby background sources (top left), and the H I spectra of PN G089.0+00.3 (bottom left), G088.8+00.9 (top right), and G089.6+00.9 (bottom right). The H I spectra of G088.46+00.0 is shown in appendix Fig. 21. The map has superimposed contours (15,25,35 K) of 1420 MHz continuum emission.

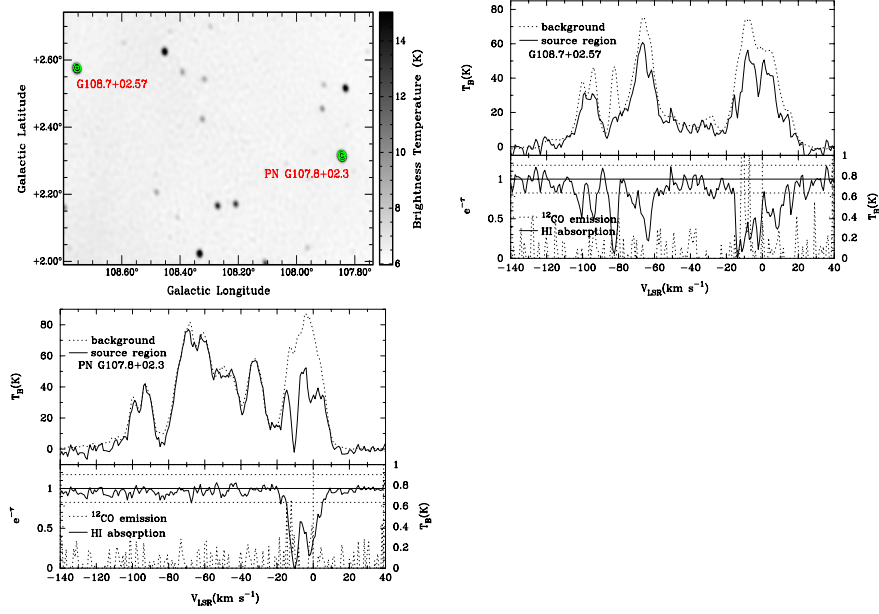


FIG. 12.— 1420 MHz continuum image of PN G107.8+02.3 and its nearby background sources (top right), and the H I spectra of PN G107.8+02.3 (bottom left), G108.7+02.57 (top right). The map has superimposed contours (20, 50, 100 K) of 1420 MHz continuum emission.

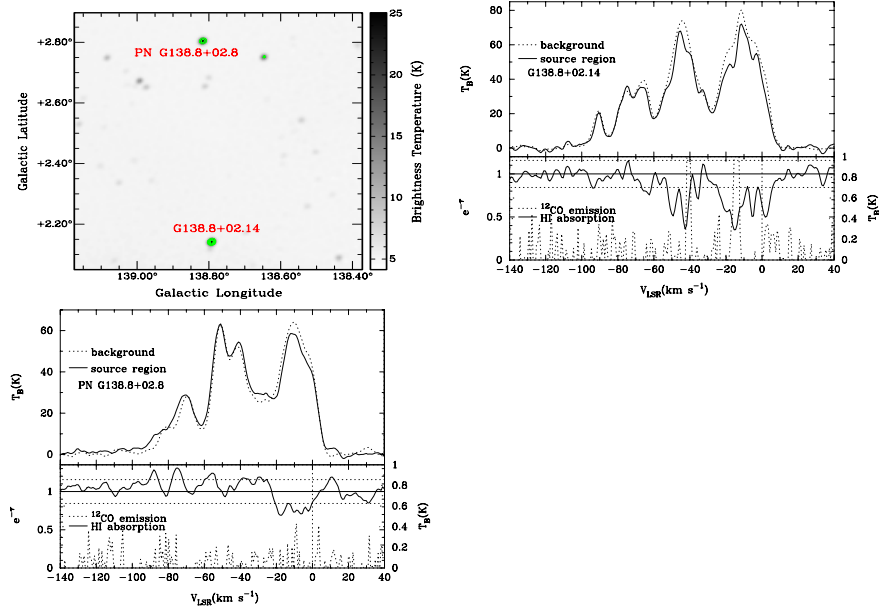


FIG. 13.— 1420 MHz continuum image of PN G138.8+02.8 and G138.8+02.4 (top left), and the H I spectra of PN G138.8+02.8 (bottom left), G138.8+02.14 (top right). The map has superimposed contours (15, 25, 35 K) of 1420 MHz continuum emission.

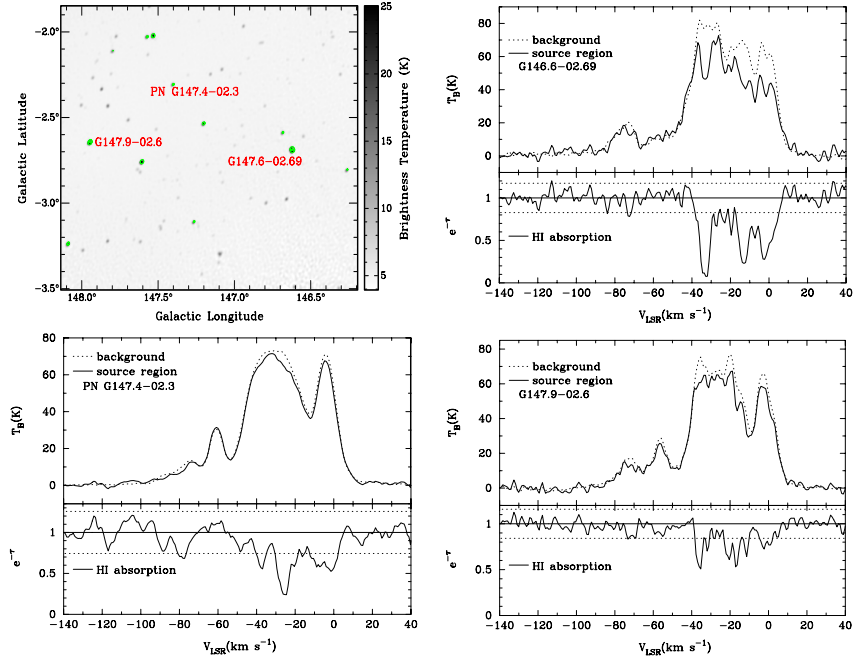


FIG. 14.— 1420 MHz continuum image of PN G147.4–02.3, and its background sources (top left), and the H I spectra of PN G147.4–02.3 (bottom left), G146.6–02.69 (top right) and G147.9–02.6 (bottom right). The map has superimposed contours (15,55 K) of 1420 MHz continuum emission.

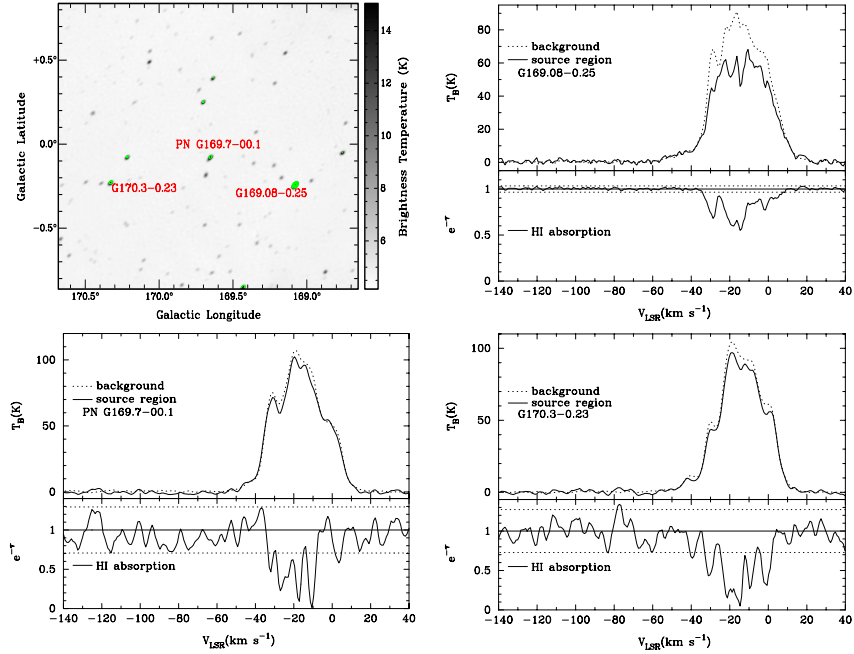


FIG. 15.— 1420 MHz continuum image of PN G169.7–00.1 and its background sources (top left), and the H I spectra of PN G169–00.1 (bottom left), G169.08–0.25 (top right) and G170.3–0.23 (bottom right). The map has superimposed contours (15,50,100 K) of 1420 MHz continuum emission.



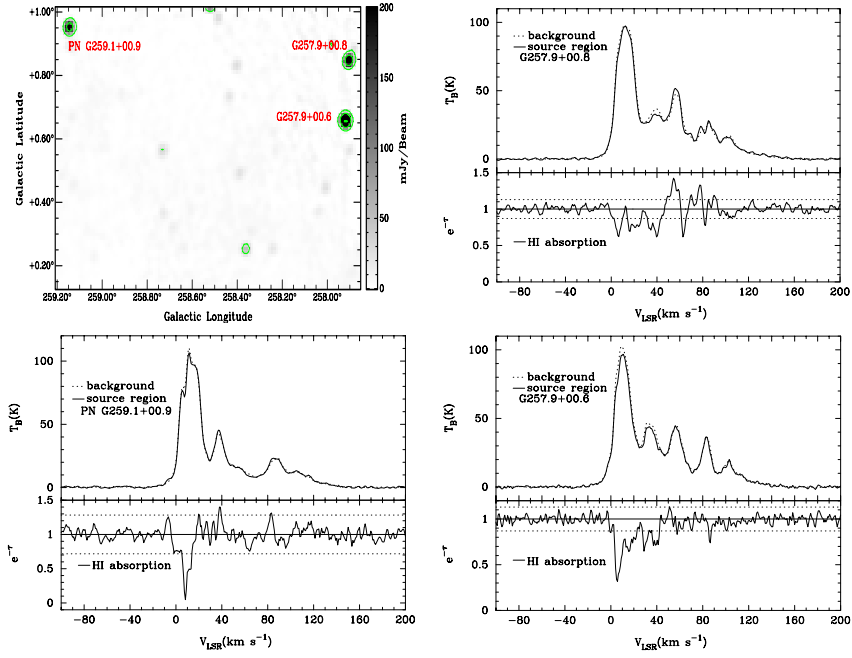


FIG. 16.— 1420 MHz continuum image of PN G259.1+00.9, and its nearby background sources (top left), and the H I spectra of PN G259.1+00.9 (bottom left), G257.9+00.8 (top right) and G257.9+00.6 (bottom right). The map has superimposed contours (0.03, 0.15, 0.5 Jy) of 1420 MHz continuum emission.

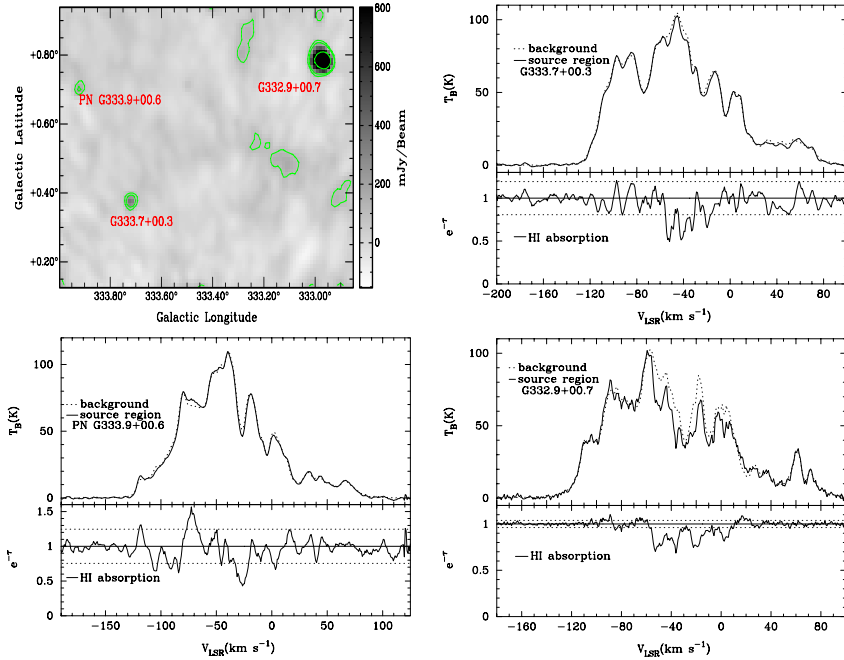


FIG. 17.— 1420 MHz continuum image of PN G333.9+00.6, and its background sources (top left), and the H I spectra of PN G333.9+00.6 (bottom left), G333.7+00.3 (top right) and G332.9+00.7 (bottom right). The map has superimposed contours (0.1, 0.18, 1.0 Jy) of 1420 MHz continuum emission.



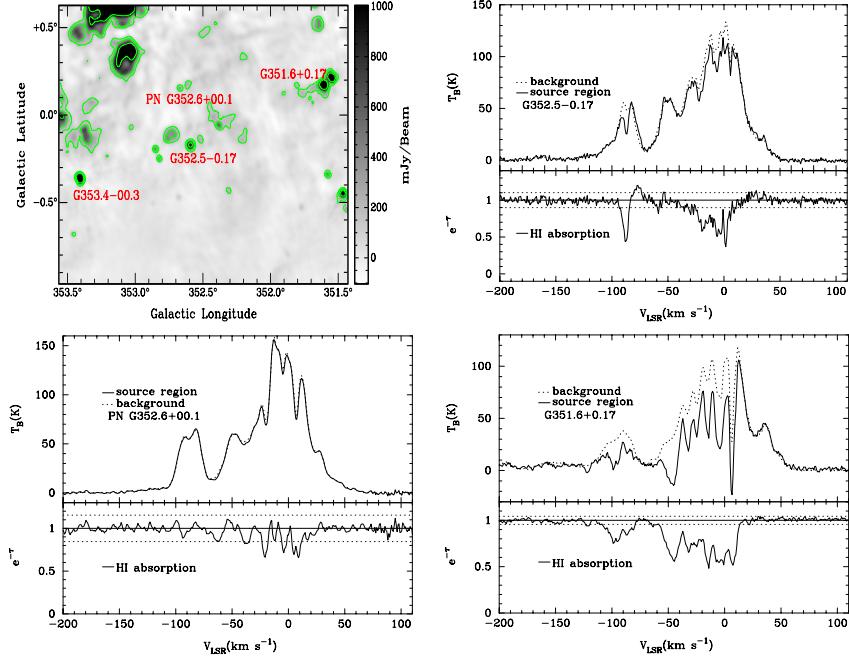


FIG. 18.— 1420 MHz continuum image of PN G352.6+00.1 and its nearby background sources (top left), and the H I spectra of PN G352.6+00.1 (bottom left), G352.5-0.17 (top right), and G351.6+0.17 (bottom right). The H I spectra of G353.4-00.3 is shown in Fig. 19. The map has superimposed contours (0.15, 0.35, 1.0 Jy) of 1420 MHz continuum emission.

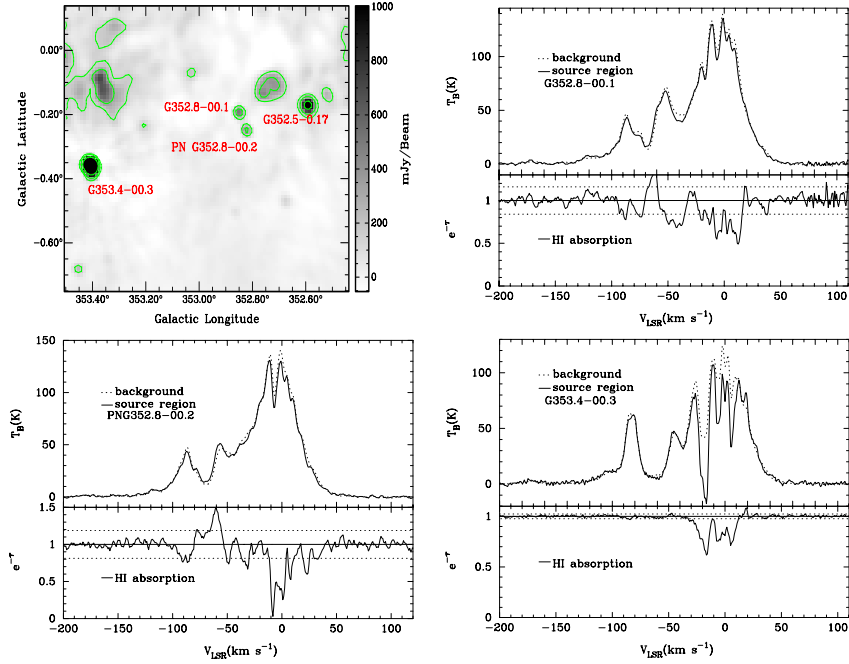


FIG. 19.— 1420 MHz continuum image of PN G352.8-00.2 and its nearby background sources (top left), and the H I spectra of PN G352.8-00.2 (bottom left), G352.8-00.1 (top right), and G353.4-00.3 (bottom right). The H I spectra of G352.5-0.17 is shown in Fig. 18. The map has superimposed contours (0.15, 0.35, 1.0 Jy) of 1420 MHz continuum emission.

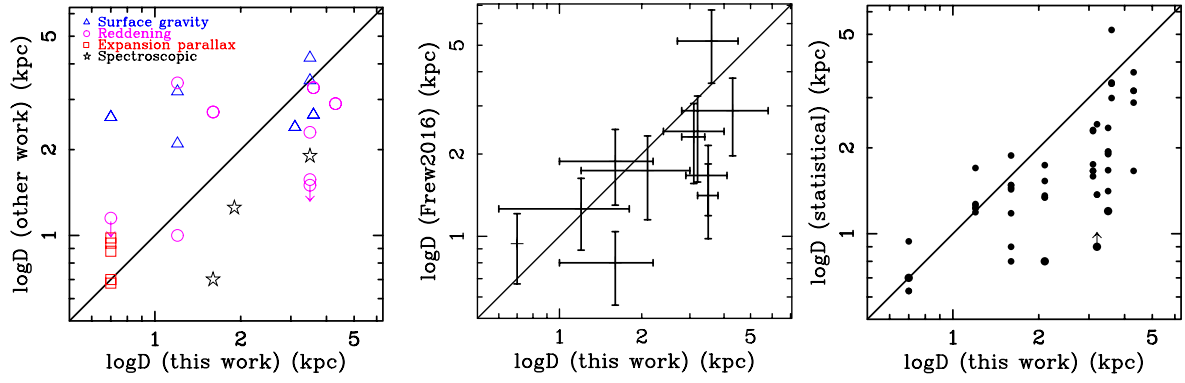


FIG. 20.— Left panel: the correlation between our work and all other work (except statistical method). Middle panel: the correlation between our work and Frew et al. (2016). Right panel: the correlation between our work and all statistical results.

## APPENDIX

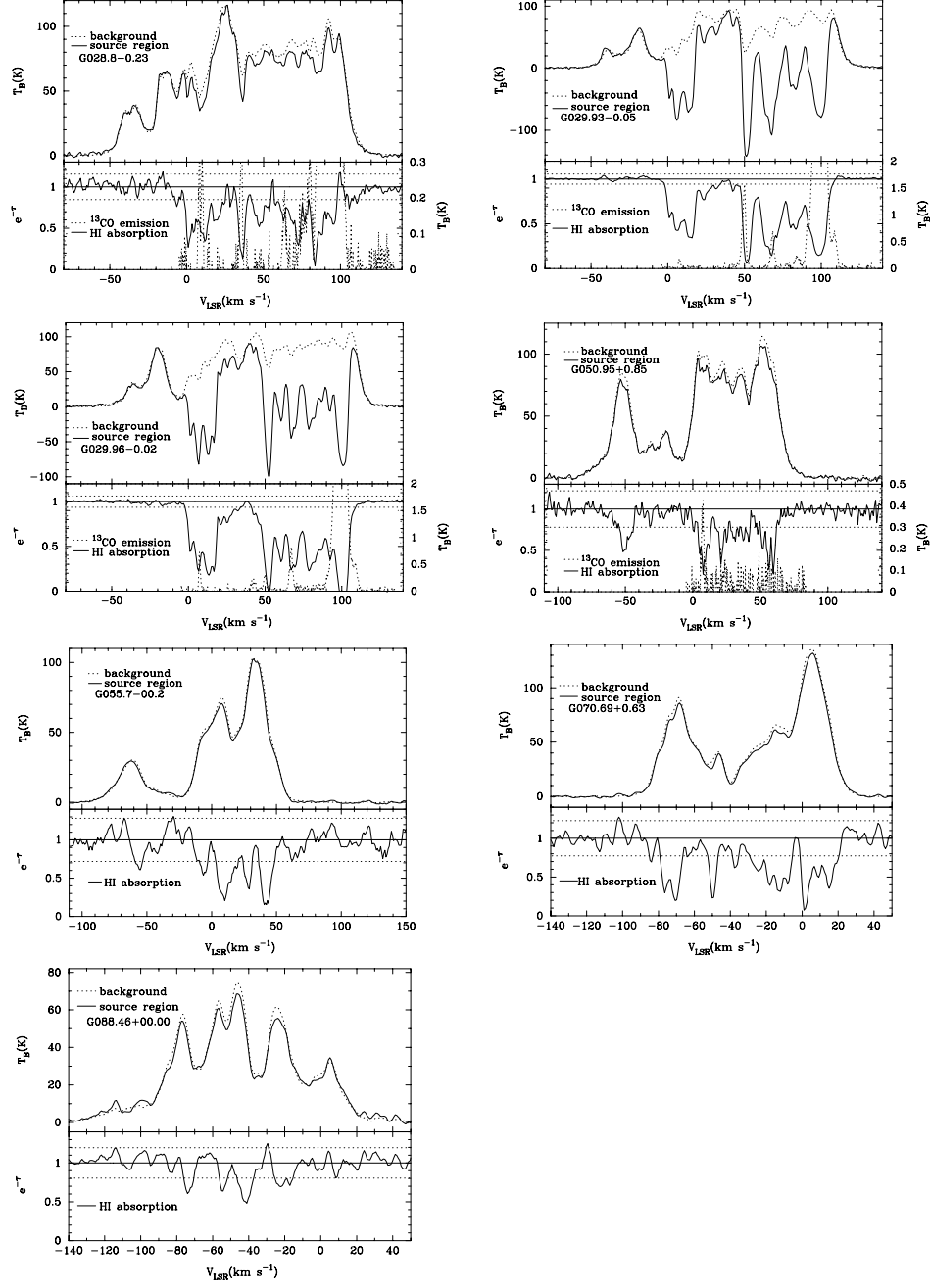


FIG. 21.— Nearby background sources are also used to measure the PN kinematic distances, the dotted horizontal lines in the lower panel of the background sources show the 3 $\sigma$  noise level.